Journal of Energy Storage 72 (2023) 108403

Contents lists available at ScienceDirect

Journal of Energy Storage

journal homepage: www.elsevier.com/locate/est

Research Papers

Co-precipitation synthesis of pseudocapacitive λ-MnO_2 for 2D MXene ($Ti_3C_2T_x$) based asymmetric flexible supercapacitor

B. Thanigai Vetrikarasan [a,b], Abhijith R. Nair [a,b], T. Karthick [b], Surendra K. Shinde [c,d], Dae-Young Kim [c], Shilpa N. Sawant [e,f], Ajay D. Jagadale [a,b,*]

[a] Centre for Energy Storage and Conversion, SASTRA Deemed University, Thanjavur 613401, Tamil Nadu, India
[b] Department of Physics, School of Electrical & Electronics Engineering, SASTRA Deemed University, Thanjavur 613401, Tamil Nadu, India
[c] Department of Biological & Environmental Science, College of Life Science and Biotechnology, Dongguk University, 32 Dongguk-ro, Biomedical Campus, Ilsandong-gu, Siksa-dong, 10326, Goyang-si, Gyeonggi-do, Republic of Korea
[d] Department of Physics, Arts, Science and Commerce College, Indapur, Pune 413106, India
[e] Chemistry Division, Bhabha Atomic Research Centre, Trombay, Mumbai 400085, India
[f] Homi Bhabha National Institute, Anushaktinagar, Mumbai 400094, India

ARTICLE INFO

Keywords:
λ-MnO_2
Nanoplate
$Ti_3C_2T_x$ MXene
Flexible hybrid supercapacitor

ABSTRACT

The rapid growth of wearable/portable electronics imposes a development of flexible, lightweight and highly efficient energy storage devices. In this work, we have synthesized λ-MnO_2 nanoplates through one step co-precipitation method and used for flexible asymmetric supercapacitor (SC). The structural, morphological and electrochemical properties of synthesized λ-MnO_2 were systematically investigated. The optical and electronic properties of λ-MnO_2 were studied using UV–vis spectroscopy and density functional theory (DFT) calculations. The pseudocapacitive λ-MnO_2 nanoplates-like electrode showed a maximum specific capacitance of 288.5 F g^{-1} at the scan rate of 5 mV s^{-1}. To check the practicability, symmetric (λ-MnO_2//λ-MnO_2) as well as asymmetric (λ-MnO_2//AC and λ-MnO_2//$Ti_3C_2T_x$ MXene) SCs were fabricated and their performances were compared. The asymmetric λ-MnO_2//$Ti_3C_2T_x$ MXene SC demonstrated a maximum energy density of 15.5 Wh kg^{-1} at the power density 1100 W kg^{-1} along with 86.3 % of capacitive retention after 5000 cycles. Besides, to confirm the suitability of these electrodes for flexible energy storage, a flexible λ-MnO_2//$Ti_3C_2T_x$ asymmetric SC was fabricated using PVA: Na_2SO_4 gel polymer electrolyte that operated in the potential window of 2 V and supplies high areal energy density of 39.9 μWh cm^{-2} at a power density of 8586 μW cm^{-2}. Therefore, the λ-MnO_2 prepared with a simple and scalable co-precipitation method may play a promising role in flexible energy storage.

1. Introduction

Electrical energy is prominent for technological development and its production through non-renewable resources greatly influences the world economy and ecological system [1]. Due to the expansion in the global need for energy, researchers have been focusing on exploring novel renewable energy sources and effective energy storage technologies [2]. Currently, electrochemical energy storage devices (EES) such as fuel cells, batteries and supercapacitors (SCs) have attracted great attention due to their good safety, reliability and eco-friendliness [3]. Amongst, SCs are mainly attracted due to their high power density and extended cycle life, exhibiting a wide range of applications in electric vehicles, communication technology, smart electronics, aircraft and smart grids [4]. Depending on the storage mechanism, SCs are classified into electric double-layer capacitors (EDLCs) and pseudocapacitors. EDLCs store electrical energy through ion adsorption/desorption while pseudocapacitors store charge via rapid redox reaction at the interface between electrode and electrolyte [5]. SCs are largely suffered from their poor energy density (ED), therefore, a significant amount of research is anticipated to develop novel electrodes and device configurations [6,7]. The ED of SC can be improved by enhancing capacitance and operating voltage according to the relation $E = (0.5) \times CV^2$, where C is capacitance and V is operating voltage. The operating voltage and thereby the energy performance can be effectively enlarged by fabricating asymmetric SCs (ASCs). The ASC is fabricated by combining two dissimilar electrodes mainly pseudocapacitive (positive) and EDLC

* Corresponding author at: Centre for Energy Storage and Conversion, SASTRA Deemed University, Thanjavur 613401, Tamil Nadu, India.
E-mail address: jagadaleajay99@gmail.com (A.D. Jagadale).

https://doi.org/10.1016/j.est.2023.108403
Received 28 February 2023; Received in revised form 14 July 2023; Accepted 15 July 2023
Available online 17 July 2023

(negative) type, exhibiting high energy density, acceptable power density and long cycle life [8]. Recently, various non-carbon negative electrodes have been prepared for asymmetric as well as hybrid SCs including VO [9], V_2O_5 [10], WO_3 [11], MXene [12], etc. The 2D MXenes have attracted great attention due to their intrinsic electrical conductivity, hydrophilicity and layered structure [13]. In our previous work, we evidenced that the hybrid SC based on 2D MXene as a negative electrode device showed superior energy and power performance as compared with the SCs fabricated using activated carbon (AC) as a negative electrode [14,15]. In our attempt of improving the ED of SCs, we chose to prepare pseudocapacitive MnO_2 as a positive electrode due to its high theoretical capacitance ($1370\,F\,g^{-1}$), multiple oxidation states, natural abundance, thermal stability and inexpensiveness [16]. The SC performance of MnO_2 depends on its crystallographic polymorphs such as α, β, γ, δ and λ-MnO_2. Amongst, the α-MnO_2 has been frequently reported for SC application, however, its operating potential window ranges typically from 0 to +0.8 V in aqueous electrolyte. On the other hand, the λ-MnO_2 demonstrates an extended potential window up to 2 V along with excellent specific capacitance. Recently, the λ-MnO_2 has emerged as a promising candidate as an electrode material for SC application due to its excellent electrochemical properties [17]. However, there are very few reports available on synthesizing λ-MnO_2 for SC application. For instance, Zhang et al. [18] synthesized λ-MnO_2 nanoparticles by using the acid leaching method that showed a maximum specific capacity of 390.7 mAh g^{-1} at 13.6 mA g^{-1}. It is observed that the λ-MnO_2 was mainly prepared using the acid leaching method which is multi-step and involves toxic chemicals. Therefore, it is highly desirable to synthesize λ-MnO_2 with a simple, scalable and cost-effective method.

With this knowledge, in the present work, we have synthesized phase pure λ-MnO_2 with chemical homogeneity using a single-step scalable co-precipitation method for the first time. This λ-MnO_2 was characterized for structural, morphological and electrochemical analyses. The band gap of the λ-MnO_2 was determined as 5.65 eV using UV–Vis spectroscopy which was in good agreement with that predicted from density functional theory (DFT) calculations. The λ-MnO_2 demonstrated a maximum specific capacitance of 288.5 F g^{-1} at the scan rate of 5 mV s^{-1}. To test the practicability, three types of aqueous SCs were fabricated and compared using λ-MnO_2, (λ-MnO_2//λ-MnO_2) $Ti_3C_2T_x$ MXene (λ-MnO_2//$Ti_3C_2T_x$) and AC (λ-MnO_2//AC) electrodes. Interestingly, the λ-MnO_2//$Ti_3C_2T_x$ ASC reflected the highest ED of 15.5 Wh kg^{-1} at the power density (PD) of 1100 W kg^{-1} which was quite higher than the ASC based on AC (λ-MnO_2//AC). Besides, the λ-MnO_2//$Ti_3C_2T_x$ ASC exhibited excellent capacitance retention of 86.3 % after 5000 cycles with coulombic efficiency (CE) maintained around 99 %. Furthermore, to understand the applicability of this device in wearable electronics, the flexible ASC was fabricated using PVA: Na_2SO_4 gel electrolyte that operates within a wider potential window of 2 V and provided a maximum areal ED of 39.9 μWh cm^{-2} at a PD of 8586.4 μW cm^{-2}.

2. Experimental section

2.1. Chemicals and materials

Manganese (II) nitrate tetrahydrate ($Mn(NO_3)_2.4H_2O$) was purchased from Alfa Aesar, UK. Analytical grade sodium hydroxide (NaOH) and sodium sulfate anhydrous (Na_2SO_4) were purchased from Sisco Research Laboratories Pvt. Ltd. (SRL), India. Hydrogen peroxide (H_2O_2) was obtained from Isochem Laboratories, India. The Ti_3AlC_2 (MAX phase) powder was procured from Jinzhou Haixin Metal Materials Co., Ltd. The 304 stainless steel (SS) with a thickness of 0.05 mm was received from Labtronics Enterprises, India.

2.2. Synthesis of λ-MnO_2

The λ-MnO_2 powder was synthesized using a single-step co-precipitation method. Initially, the aqueous solution of 0.3 M $Mn(NO_3)_2.4H_2O$ was prepared, to this solution, the NaOH pellets were added (0.67 M). After 5 min, 30 ml of H_2O_2 (9.79 M) was added and the mixture was stirred for 30 min at 200 rpm. Then, the brown-black precipitated solution was centrifuged for several cycles by using DI water at 8000 rpm until pH becomes neutral. Finally, the sediment was dried at 70 °C overnight to get λ-MnO_2 powder.

2.3. Synthesis of 2D MXene ($Ti_3C_2T_x$)

The $Ti_3C_2T_x$ MXene was prepared as per our previous work [14]. Briefly, 25 ml of concentrated HCl was taken in a Teflon container and to this, 1 g of LiF was added. The mixture was maintained at 45 °C under constant stirring (200 rpm). Furthermore, 1 g of MAX phase (Ti_3AlC_2) powder was slowly added to this solution and the reaction was maintained for 24 h. After, a solution was centrifuged with DI water for 7 cycles at 9000 rpm to remove the unreacted MAX phase and neutralize the pH. Then the sediment was dissolved in 100 ml of DI water and ultrasonicated for 30 min under an Ar atmosphere. Finally, the solution was centrifuged at 2000 rpm for 30 min, to obtain black ink-like dispersion of $Ti_3C_2T_x$ MXene. This ink is not stable for a longer duration of time and maybe oxidized in ambient conditions. Therefore, in the present work, freshly prepared ink was used for coating. Its life can also be extended by storing it in sealed argon-filled vials as well as by keeping it away from the light [19].

2.4. Fabrication of electrodes and SCs

The λ-MnO_2 or AC electrodes were prepared by making a homogeneous slurry of active material (λ-MnO_2 or AC), acetylene black, and polyvinylidene fluoride (PVDF) in the ratio of 8:1:1 in N-Methyl-2-pyrrolidone (NMP) solvent. The slurry was coated on stainless steel (SS) substrate (1 × 1 cm^2) followed by drying at 80 °C overnight. The active masses of λ-MnO_2 and AC electrodes were 0.62 and 1.3 mg cm^{-2}, respectively. To prepare $Ti_3C_2T_x$ MXene negative electrode, the ink-like dispersion was centrifuged at 10,000 rpm for 30 min and obtained sediment was coated on SS substrate (1 × 1 cm^2) and dried at 70 °C overnight in a vacuum oven. Both symmetric and asymmetric SCs were fabricated using a Swagelok cell. A symmetric SC was assembled by taking two identical λ-MnO_2 electrodes separated by a soaked separator (Whatman filter paper soaked in 1 M of Na_2SO_4 solution). Asymmetric (λ-MnO_2//$Ti_3C_2T_x$ MXene and λ-MnO_2//AC) SCs were fabricated using λ-MnO_2 as a positive electrode and $Ti_3C_2T_x$ MXene or AC as a negative electrode. The flexible λ-MnO_2//$Ti_3C_2T_x$ MXene ASC device was fabricated by sandwiching PVA: Na_2SO_4 gel electrolyte in between λ-MnO_2 and $Ti_3C_2T_x$ MXene-coated SS flexible electrodes. The gel electrolyte was prepared as follows, 5 g of PVA was added in 45 ml of DI water and the solution was continuously stirred and maintained at 90 °C until a clear and transparent gel-like substance was formed. To this, 15 ml of 1 M Na_2SO_4 solution was dropwise added at room temperature to obtain gel electrolyte.

2.5. Characterization

The X-ray diffraction (XRD) patterns were recorded by using an X-ray diffractometer (X'Pert^3, Panalytical, Netherlands). The elemental analyses of the samples were performed by energy-dispersive X-ray spectroscopy (XFlash, Bruker, Germany) and X-ray photoelectron spectroscopy (XPS) (K-Alpha, Thermo Fisher Scientific, USA). The specific surface area and pore size distribution were measured using Brunauer–Emmett–Teller (BET) technique (ASAP 2020, Micromeritics, USA). The optical measurement was done via Ultraviolet-visible (UV–Vis) spectroscopy (Carry 60, Agilent Technologies Inc., USA). The morphological characteristics were obtained using a field emission scanning electron microscope (FESEM) (ZEISS, USA) and transmission electron microscope (TEM) (JSM2100, JEOL, Japan). The electrochemical performance of individual electrodes was examined in the

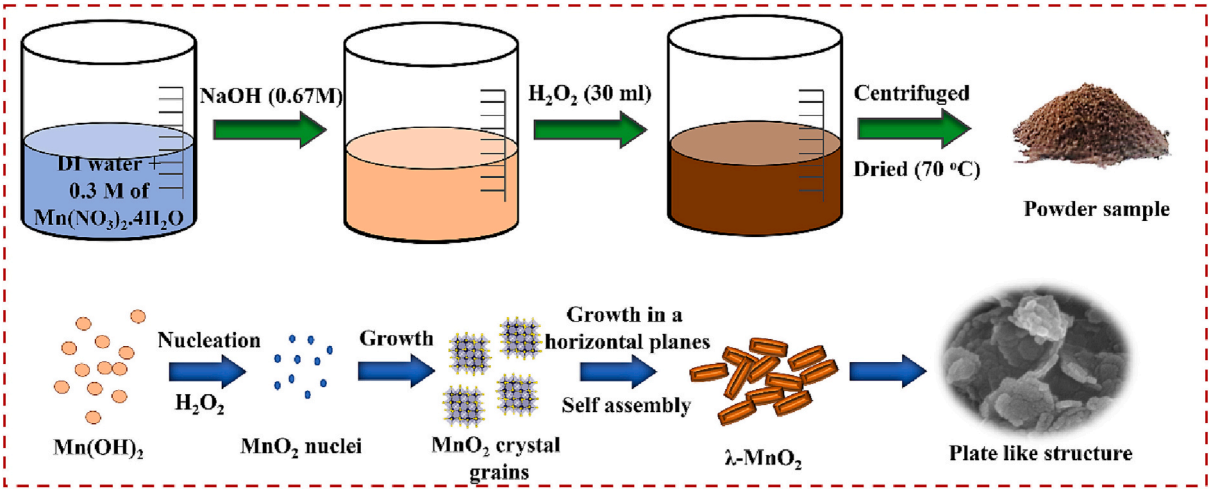

Fig. 1. Schematic of material formation mechanism.

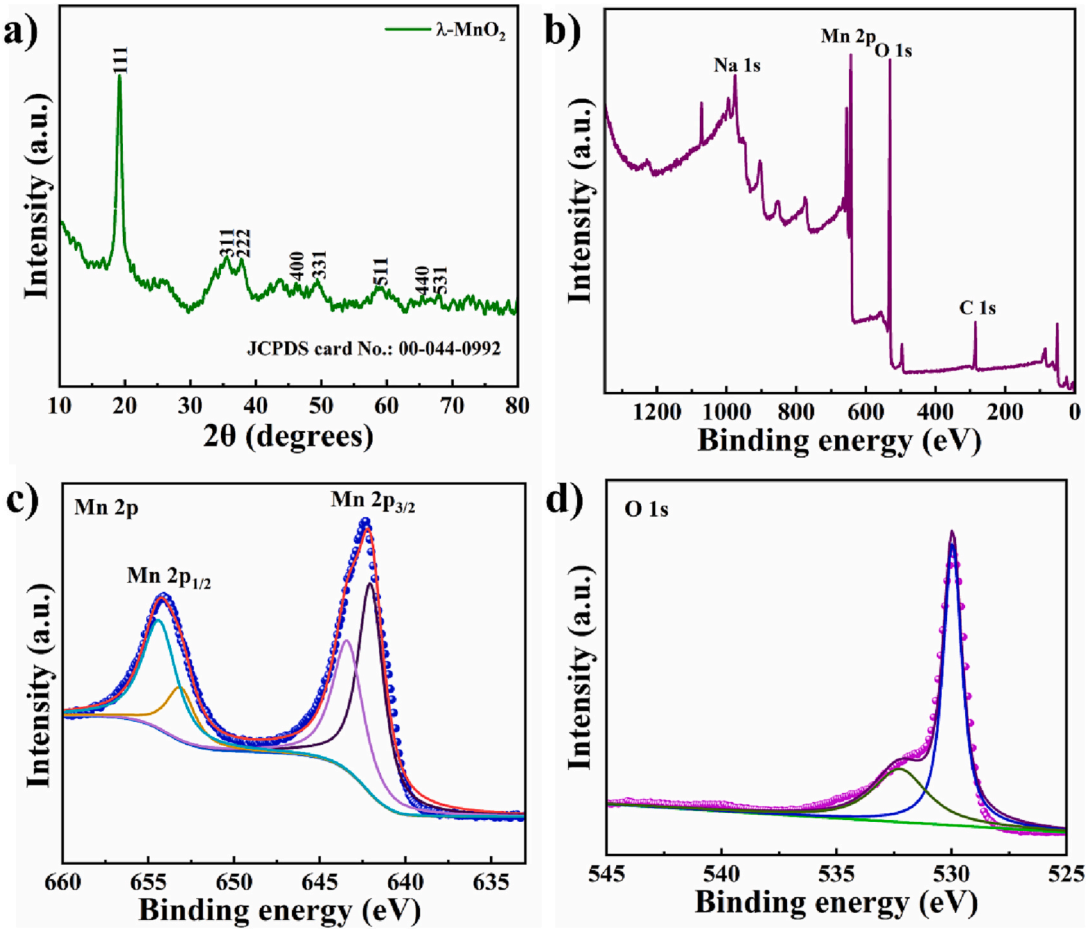

Fig. 2. (a) XRD pattern of λ-MnO_2; (b) XPS survey spectrum and core level spectra of (c) Mn 2p and (d) O 1 s for λ-MnO_2.

three-electrode system using cyclic voltammetry (CV), galvanostatic charge-discharge (GCD), and electrochemical impedance spectroscopy (EIS) techniques via Biologic SP-150 electrochemical workstation. The λ-MnO_2 or $Ti_3C_2T_x$ MXene or AC-coated SS, coiled platinum and Ag/AgCl were used as working, counter, and reference electrodes, respectively. All electrochemical tests were carried out in 1 M Na_2SO_4 aqueous electrolyte. The EIS study was performed in the frequency range from 0.1 Hz to 1 MHz with an AC amplitude of 10 mV at open circuit voltage.

3. Result and discussion

3.1. Formation mechanism of λ-MnO_2

The synthesis procedure along with the materials formation mechanism is illustrated in Fig. 1. When Mn^{2+} ions from manganese nitrate solution react with sodium hydroxide, the $Mn(OH)_2$ precipitation is formed. Furthermore, the addition of H_2O_2 oxidizes Mn species to form

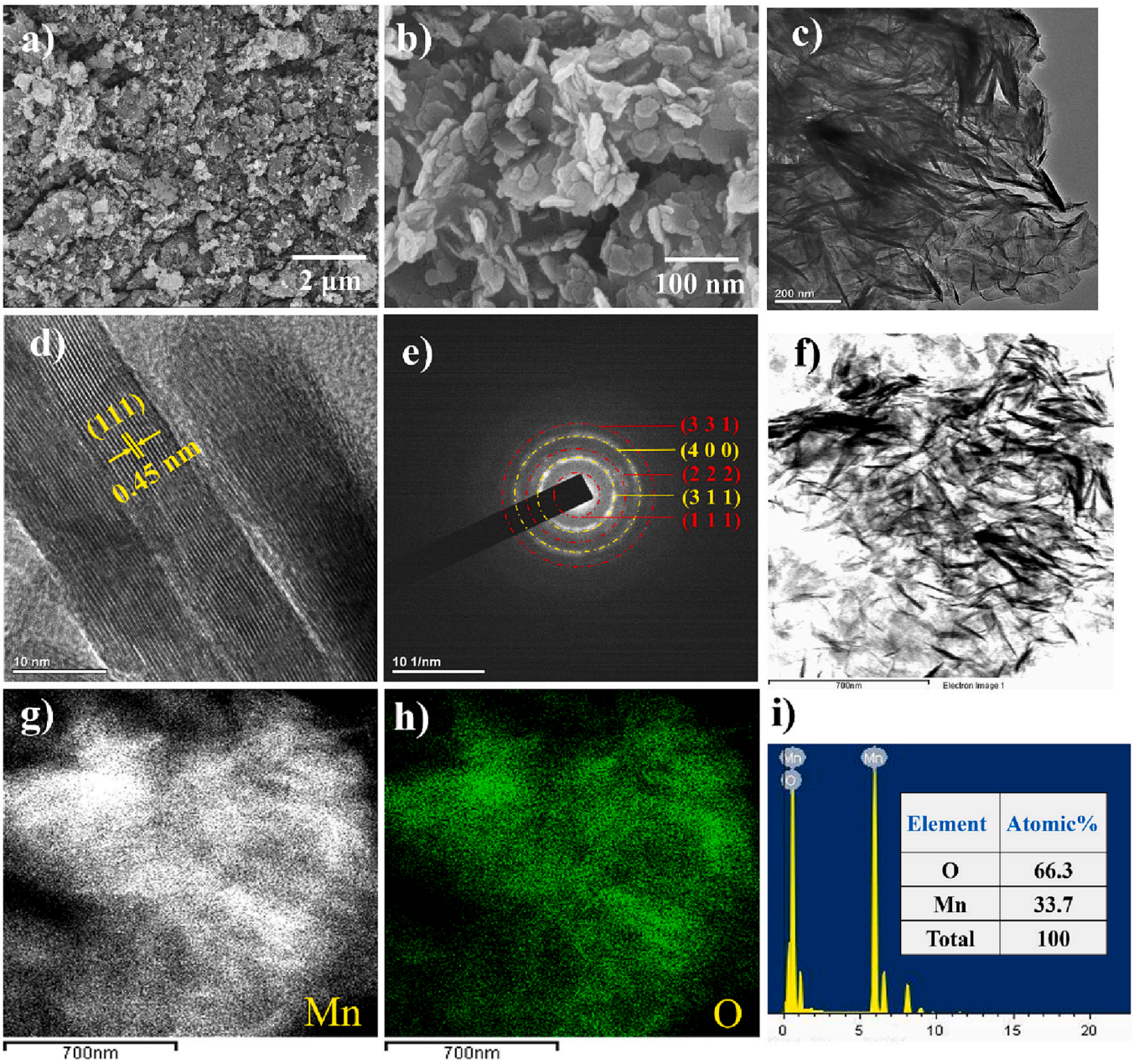

Fig. 3. FESEM images of λ-MnO_2 at (a) lower (×10,000) and (b) higher (×1,50,000) magnifications; (c) TEM and (d) HRTEM images of λ-MnO_2; e) SAED pattern of λ-MnO_2; The electronic image (f) and elemental mapping for (g) Mn and (h) O elements; (i) The EDS spectrum of λ-MnO_2.

λ-MnO_2 nuclei as per the reaction depicted below. These nuclei grow to form MnO_2 crystal grains which further evolve into horizontal planes via self-assembly to form λ-MnO_2 nanoplates-like microstructure.

$$Mn(NO_3)_2.4H_2O + 2NaOH + H_2O_2 \rightarrow MnO_2 + 2NaNO_3 + 4H_2O \quad (1)$$

3.2. Structural and morphological analyses

The crystal structure, phase and purity of the prepared powder sample were analyzed using the XRD pattern as shown in Fig. 2a. Diffraction peaks corresponding to 2θ values of 19.2, 35.6, 37.8, 46.1, 49.3, 58.8, 65.4, and 68.0° can be indexed to miller indices of (111), (311), (222), (400), (331), (511), (440), and (531), respectively of the cubic λ-MnO_2. The XRD pattern of λ-MnO_2 was in good agreement with JCPDS card no. 00-044-0992. Moreover, the XPS analysis was performed to confirm the elemental composition and oxidation state of the λ-MnO_2 sample. The survey spectrum confirmed the presence of Mn, O, Na, and C elements with atomic percentages of 22.7, 53.9, 3.7 and 19.8 %, respectively (Fig. 2b). The high-resolution Mn 2p core level spectrum depicts two major peaks at 642.68 and 653.58 eV, corresponding to Mn $2p_{3/2}$ and Mn $2p_{1/2}$, respectively (Fig. 2c). The spin energy separation between these levels was ~11 eV, confirming the presence of the Mn^{4+} state. Besides, the Mn $2p_{3/2}$ peak can be split at 642.08 and 643.48 eV, indicating the co-existence of Mn^{3+} and Mn^{4+} oxidation states, corresponding to Mn_2O_3 and MnO_2, respectively [20]. Also, in Mn $2p_{1/2}$ peak, two peaks situated at 653.18 and 654.38 eV confirm the presence of mixed oxidation states (Mn^{4+} and Mn^{3+}), respectively [21]. The O 1s spectrum can be deconvoluted into two components at 529.98, and 531.58 eV which may be attributed to the characteristic metal-oxygen bonds (Mn–O–Mn) and hydroxyl groups (Mn–O–H), respectively (Fig. 2d) [22].

The morphology of λ-MnO_2 was examined using field emission

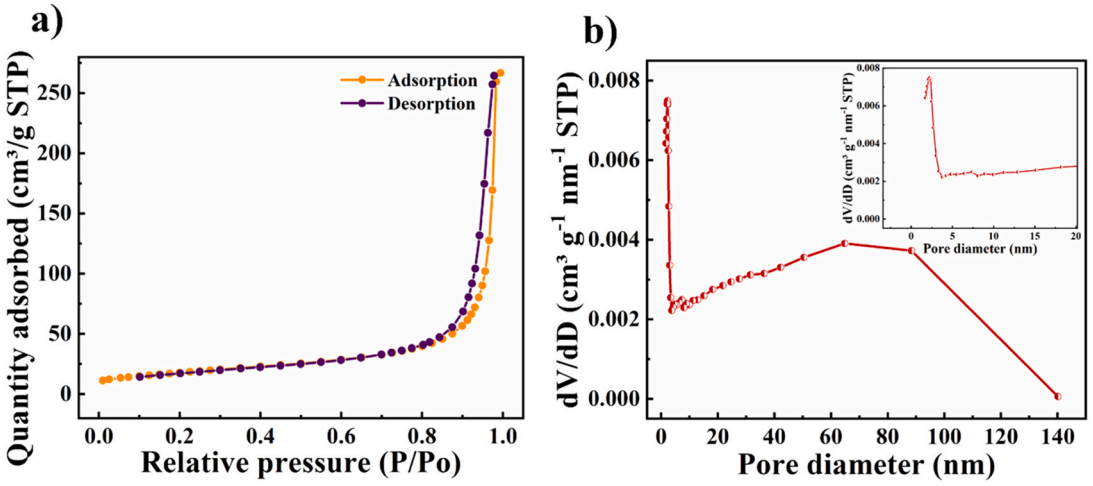

Fig. 4. (a) BET analysis and (b) pore size distribution of λ-MnO_2 (inset: zoomed region).

scanning electron microscopy (FESEM) as shown in Fig. 3a and b, demonstrating irregularly distributed, self-assembled and porous nanoplates-like structure. This type of microstructure may provide high surface area, numerous electrochemically active sites and reduced ionic pathways for rapid surface redox reactions during the charging-discharging process [23]. As shown in the elemental mapping and EDS

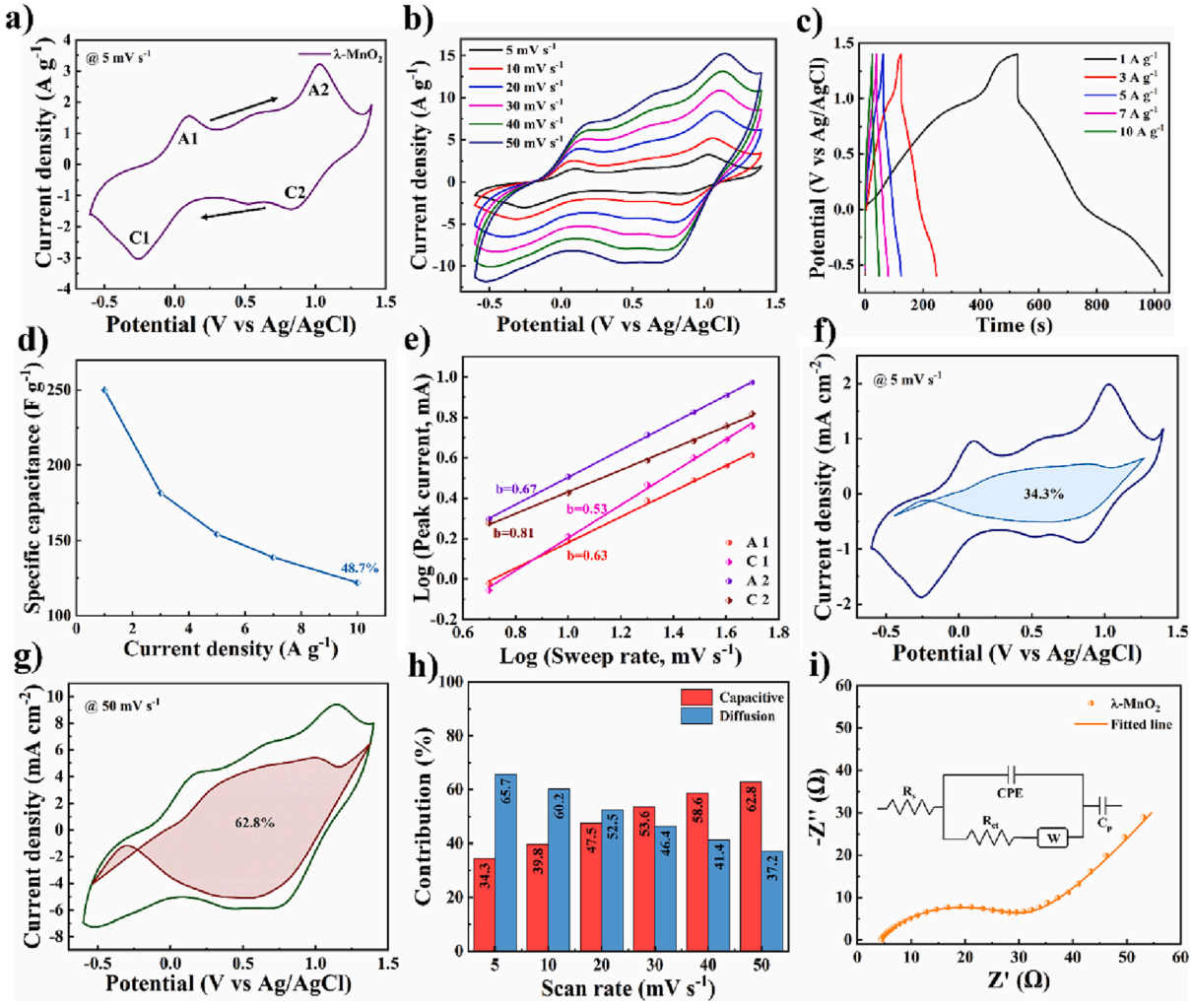

Fig. 5. (a) CV curve of λ-MnO_2 at 5 mV s^{-1}; (b) CV curves of λ-MnO_2 at different scan rates; (c) GCD curves of λ-MnO_2 at different current densities; (d) The variation of specific capacitance and current density for λ-MnO_2; (e) The variation of peak current versus the scan rate; The deconvolution of surface capacitive and diffusion-controlled contributions at the scan rate (f) 5 and (g) 50 mV s^{-1} for λ-MnO_2 electrode; (h) Contributions at various scan rates; (i) Nyquist plot for λ-MnO_2 (inset: equivalent circuit).

spectrum of λ-MnO_2 (fig. S1), the Mn and O were present and uniformly distributed throughout the surface. The low magnification TEM image of λ-MnO_2 supports the formation of ultrathin nanoplates-like microstructure Fig. 3c. As shown in the high-resolution TEM (HRTEM) image, the d-spacing of 0.45 nm belongs to the (111) plane of λ-MnO_2, matching well with the value obtained by XRD analysis (Fig. 3d). The SAED pattern demonstrates the polycrystalline nature of λ-MnO_2 as shown in Fig. 3e. The elemental mapping images and EDS spectrum are shown in Fig. 3f-i, inferring uniform distribution and presence of both Mn and O in the λ-MnO_2.

3.3. Optical and theoretical studies

The electrical conductivity of the electrode material is one of the important demanding properties for SC application. The electronic band gap gives a good estimate of material whether it is conducting or semiconducting or insulating. Therefore, the electronic properties of λ-MnO_2 were studied using UV–visible absorption spectroscopy and DFT calculations as shown in Fig. S2. The experimental band gap was estimated using the Tauc relation $\alpha h\nu = B(h\nu - E_g)^n$, where α, hν, B and E_g are the absorption coefficient, photon energy, proportionality constant, and optical band gap, respectively. The E_g is a direct allowed band gap for n = ½. The extrapolation of the straight line in the plot decides a band gap which was found to be 5.65 eV, indicating poor conducting behavior of λ-MnO_2. Besides experimental findings, the density of states (DOS) spectrum and band structures of MnO_2 were explored to find the electron density distribution within the system and the band gap energy using an open-source quantum espresso software package [24]. The single point energy of MnO_2 in an orthorhombic face-centered cubic lattice was obtained by using ultrasoft pseudopotentials (USPP) for Mn and O atoms. The number of k-points and cut-off for the wave function and charge were identified by repeated energy convergence of MnO_2 up to 0.0001 Ry. The self-consistent field energy of MnO_2 is predicted as −1094.48339738 Ry. The calculated band gap energy of MnO_2 was 5.6 eV which was in good agreement with the experimental band gap. The density of states spectrum (Fig. S2c) shows that the up-spin configuration of oxygen occupies the highest energy of the valance band and the lowest energy of the conduction band is occupied by the up-spin configuration of both Mn and O atoms. The band structure (Fig. S2d) evidenced the direct band gap of λ-MnO_2 as the electrons in the HOMO and LUMO occur at the same value of momentum.

The nitrogen (N_2) adsorption–desorption isotherm of λ-MnO_2 was carried at Standard Temperature and Pressure (STP). It shows a significant hysteresis loop between relative pressure (P/P_0) of 0.8 and 1.0 which reveals the capillary condensation with type-IV isotherm and H3-type hysteresis loop, demonstrating the mesoporous structure of λ-MnO_2 (Fig. 4a) [25]. This type of loop is normally observed for non-rigid aggregates of plate-like particles, supporting the formation of nanoplates-like morphology of the λ-MnO_2 [26]. Moreover, the BET-specific surface area and the pore volume of λ-MnO_2 were estimated as 64.13 $m^2\ g^{-1}$ and 0.409 $cm^3\ g^{-1}$, respectively. The pore size distribution of the λ-MnO_2 was obtained from desorption isotherms using the Barret–Joyner–Halenda (BJH) method (Fig. 4b), indicating that the pore size is mainly concentrated at 2.36 nm. Also, the small amount of pore sizes was centered at around 70 nm, displaying the significant macroporosity in the material. The high specific surface area and the meso-macro porous structure of λ-MnO_2 may provide numerous electrochemically active sites and hassle-free ionic transport during the charging-discharging process.

3.4. Electrochemical analysis

The electrochemical performance was tested using a three-electrode system via CV, GCD, and EIS techniques as shown in Fig. 5. The CV curve of λ-MnO_2 within the potential window of −0.6 to 1.4 V vs Ag/AgCl at the scan rate of 5 mV s^{-1} in 1 M Na_2SO_4 electrolyte is shown in Fig. 5a, demonstrating two clear oxidation and reduction peaks corresponding to insertion-extraction of Na^+ ions in the 8a and 16c lattice sites of λ-MnO_2 (Eqs. (2) and (3)) [18]. It is also noted that the oxygen and hydrogen evolution was not taken place during the charging-discharging of λ-MnO_2.

$$[]_{8a16c}[Mn_2]_{16d}[O_4]_{32e} \rightarrow [Na_x]_{8a16c}[Mn_2]_{16d}[O_4]_{32e} \quad (2)$$

$$[Na_x]_{8a16c}[Mn_2]_{16d}[O_4]_{32e} \rightarrow [Na_x]_{8a}[Na_y]_{16c}[Mn_2]_{16d}[O_4]_{32e} \quad (3)$$

As shown in Fig. 5b, when the scan rate increased, the oxidation and reduction peaks shifted toward more positive and negative sides, respectively due to the internal resistance of the electrode [27]. The specific capacitance of λ-MnO_2 was estimated to be 288.5 F g^{-1} at the scan rate of 5 mV s^{-1}. Also, this electrode showed an extended potential window of −0.4 to 1.6 V in 1 M Na_2SO_4 electrolyte. Moreover, the charging and discharging behavior of λ-MnO_2 was investigated using the GCD technique. Fig. 5c shows GCD curves for λ-MnO_2 electrode at current densities ranging from 1 to 10 A g^{-1}. The non-linear GCD curves may be attributed to the pseudocapacitive behavior of the electrode [28]. The iR drop at the beginning of the charging as well as the discharging cycle is mainly due to the internal resistance of λ-MnO_2. Furthermore, the value of specific capacitance was calculated to be 250 F g^{-1} at the current density of 1 A g^{-1}. This value was quite higher when compared with the reported λ-MnO_2 and equivalent to other polymorphs of MnO_2 (Table S1). This improved value of capacitance is attributed to the nanoplates-like morphology and the high specific surface area of the λ-MnO_2 electrode [29]. The values of specific capacitance were estimated to be 250, 181.6, 154.2, 138.8, and 121.9 F g^{-1} at the current densities of 1, 3, 5, 7, and 10 A g^{-1}. As shown in Fig. 5d, the capacitance retention was shown to be 48.7 % even at the higher current density of 10 A g^{-1}, depicting the appreciable rate capability of the electrode.

To explore the charge storage mechanism, the correlation between scan rate (*v*) and peak current (i) was studied using the power law Eq. (4),

$$i = a \times v^b \quad (4)$$

where a and b are constants. The b-value of 1 indicates a capacitive or surface-controlled process and b = 0.5 intends the diffusion-controlled process. The calculated b-values of 0.63, 0.67, 0.81, and 0.53 corresponding to A1, A2, C1 and C2 (anodic and cathodic peaks), respectively reveal that the charge storage is neither dominated by surface-controlled nor diffusion-controlled processes (Fig. 5e). This demonstrates the current response is controlled by both mixed surface and diffusion-controlled processes. Moreover, to separate the rapid capacitive and slow diffusion-controlled charge storage contributions, the following equation was used (5),

$$i(V) = k_1 v + k_1 v^{0.5} \quad (5)$$

where 'i(V)' is the current response and 'v' is the scan rate. The 'k_1' and 'k_2' are constants corresponding to rapid and slow kinetic processes, respectively. As shown in Fig. 5f and g, the λ-MnO_2 nanoplates electrode demonstrated a capacitive contribution of 34.3 and 62.8 % at the scan rates of 5 and 50 mV s^{-1}. The capacitive contribution increases with the increase in scan rate (Fig. 5h), indicating a fast kinetic process of λ-MnO_2.

The electrical properties of λ-MnO_2 were examined using three electrode system via EIS. As shown in the Nyquist plot (Fig. 5i), the depressed semicircle was observed in the high-frequency region and a straight line in the low-frequency region. The diameter of the semicircle provides a charge transfer resistance (R_{ct}) and the straight line in the low-frequency region signifies the frequency-dependent diffusion-controlled Warburg impedance (W_0). The intercept on the real axis (Z') implies the solution resistance (R_s), relating to the conductivity of the electrolyte and thicknesses of the active material as well as the separator

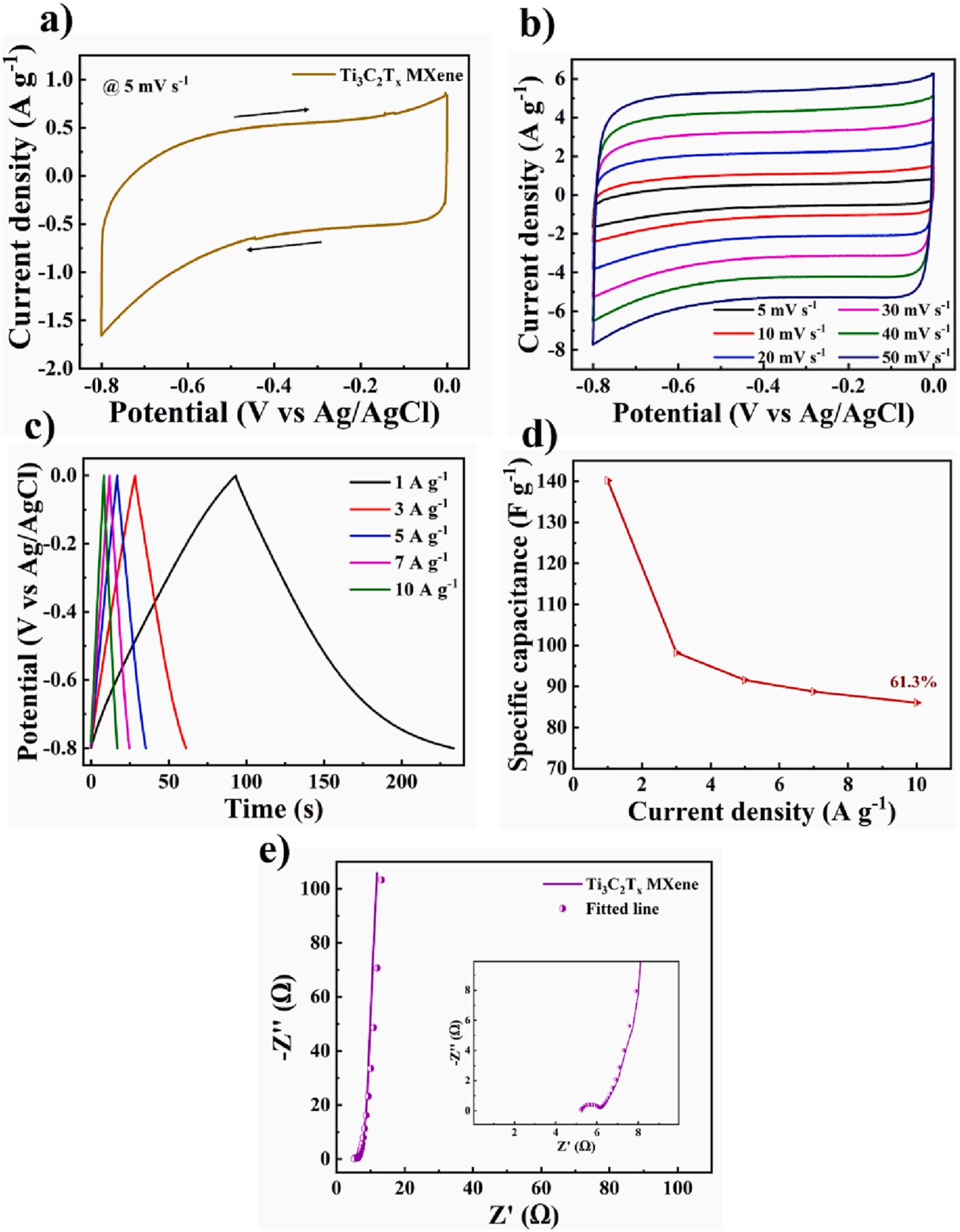

Fig. 6. (a) CV curve at 5 mV s^{-1} and (b) different scan rates for $Ti_3C_2T_x$ MXene electrode; (c) GCD curves of λ-MnO_2 at different current densities; d) The variation of specific capacitance versus current density of $Ti_3C_2T_x$ MXene electrode; e) Nyquist plot for $Ti_3C_2T_x$ MXene electrode (inset: magnified high-frequency region).

[30,31]. The R_{ct} is contributed by electronic and ionic resistances. The electronic resistance includes the intrinsic resistance of the active material, contact resistance between materials particles and resistance between the current collector and active material. The ionic resistance is the resistance experienced by the electrolyte ions inside the pores of the electrode, depending on the conductivity of the electrolyte, pore structure and thickness of active material. The equivalent circuit containing R_s, R_{ct}, CPE (constant phase element), C_p and W_0 circuit elements corresponding to experimental data is shown in the inset of Fig. 5i. The CPE is a non-intuitive circuit element considered for the inhomogeneity in the surface and porous nature of the electrode material. The R_s and R_{ct} values for λ-MnO_2 electrode were estimated as 4.25 and 27.24 Ω, respectively which were relatively smaller when compared with the reported values for MnO_2 [32], indicating good conducting behavior of λ-MnO_2 nanoplates.

The electrochemical performance of $Ti_3C_2T_x$ MXene was tested via a three-electrode system in 1 M Na_2SO_4 electrolyte. As shown in the CV curve (Fig. 6a), the quasi-rectangular shape indicates the pseudocapacitive nature of the $Ti_3C_2T_x$ MXene electrode [33]. The possible electrochemical reaction corresponding to the charging-discharging of the $Ti_3C_2T_x$ electrode is shown below (6),

$$Ti_3C_2T_x + xNa^+ + xe^- \leftrightarrow Na_xTi_3C_2T_x \quad (6)$$

The $Ti_3C_2T_x$ electrode demonstrated a maximum specific capacitance of 71.2 F g^{-1} at the scan rate of 5 mV s^{-1} with an extended negative potential window from 0 to −0.8 V. When the scan rate increased, the current under the CV curve also increased, indicating excellent capacitive behavior of the $Ti_3C_2T_x$ MXene electrode (Fig. 6b) [34]. GCD curves at different current densities are shown in Fig. 6c, depicting slightly deviated linear charging and discharging curves, suggesting the pseudocapacitive behavior of the $Ti_3C_2T_x$ MXene electrode. The maximum value of specific capacitance was obtained as 89.2 F g^{-1} at the current density of 1 A g^{-1}. The variation of specific capacitance and current density is shown in Fig. 6d, inferring good capacitance retention and hence the rate capability of $Ti_3C_2T_x$ MXene electrode even at the high current density of 10 A g^{-1}. This rate capability is mainly attributed to the superior electrical conductivity of the $Ti_3C_2T_x$ MXene electrode [35]. Furthermore, the electrical properties of the $Ti_3C_2T_x$ MXene electrode were tested using EIS as shown in the Nyquist plot (Fig. 6e). The R_s and R_{ct} values for the $Ti_3C_2T_x$ MXene electrode were estimated as 5.0 and 1.3 Ω, respectively. These lower values are ascribed to the superior electrical conductivity and hassle-free charge transfer reactions of the $Ti_3C_2T_x$ MXene electrode. The vertical spike in the low-frequency region indicates the capacitive behavior of the MXene electrode. This type of highly capacitive and kinetically fast negative electrode exhibits a promising role in the fabrication of ASCs. Similarly, the performance of commercially available AC electrodes was tested using CV, GCD and EIS techniques in 1 M Na_2SO_4 electrolyte (Fig. S3), exhibiting a maximum specific capacitance of 70.5 F g^{-1} at the current density of 1 A g^{-1} and relatively lower values of solution (4.092 Ω) and charge transfer (2.843 Ω) resistances.

To test the electrochemical behavior of materials in the device form, different configurations were made including symmetric and asymmetric SCs. The electrodes were prepared by coating active materials on the flexible SS substrate (1 × 1 cm^2) and the electrolyte (1 M Na_2SO_4) was incorporated using soaked filter paper. The symmetric SC was fabricated using two identical λ-MnO_2 electrodes, whereas two types of ASCs were fabricated using two different negative electrodes namely $Ti_3C_2T_x$ MXene and AC to effectively utilize the capacitances of both positive and negative electrodes by balancing charges on both electrodes as per the following Eq. (7) [15],

$$C_+V_+m_+ = C_-V_-m_- \quad (7)$$

where, C_+ and C_- are specific capacitances, V_+ and V_- potential windows and m_+ and m_- are actives masses of positive and negative electrodes, respectively. The schematic of a representative λ-MnO_2//$Ti_3C_2T_x$ ASC is shown in Fig. 7. The CV curves of symmetric λ-MnO_2//λ-MnO_2, asymmetric λ-MnO_2//AC and λ-MnO_2//$Ti_3C_2T_x$ SCs at the scan rate of 5 mV s^{-1} are shown in Fig. 8a, displaying a wide potential window (0 to 2.2 V) and enhanced area under the curve of λ-MnO_2//$Ti_3C_2T_x$ ASC. The values of specific capacitance for λ-MnO_2//λ-MnO_2, λ-MnO_2//AC, and λ-MnO_2//$Ti_3C_2T_x$ SCs were obtained as 11, 24.7, and 28.5 F g^{-1} at the scan rate of 5 mV s^{-1}, respectively. The enhanced specific capacitance of λ-MnO_2//$Ti_3C_2T_x$ ASC may be attributed to the high specific capacitance contributed by the 2D $Ti_3C_2T_x$ MXene negative electrode and the synergic effect between both positive and negative electrodes. The relatively poor specific capacitance of λ-MnO_2//AC ASC may be due to the increased diffusional resistance associated with the AC electrode in the device form. As shown in Fig. 8b, when the scan rate increased from 5 to 50 mV s^{-1}, the shape of CV curves doesn't change significantly, implying the superior rate capability of the λ-MnO_2//$Ti_3C_2T_x$ MXene ASC [36]. The GCD curves of λ-MnO_2//λ-MnO_2, λ-MnO_2//AC and λ-MnO_2//$Ti_3C_2T_x$ SCs at the scan rate of 1 A g^{-1} are shown in Fig. 8c. The specific capacitances calculated from GCD curves were 3.3, 13.2, and 23.1 F g^{-1} at the current density of 1 A g^{-1}, respectively. Each curve demonstrates a significant iR drop, however, the iR drop of λ-MnO_2//$Ti_3C_2T_x$ MXene ASC was relatively small which may be due to the excellent conductivity contributed by the $Ti_3C_2T_x$ MXene electrode. To test the rate capability of all devices, the GCD was performed at different current densities ranging from 1 to 7 A g^{-1} (Fig. 8d and S4). The variation of specific capacitance versus current density is shown in Fig. 8e. The capacitance retentions at the higher current density of 7 A g^{-1} were obtained as 2.98, 5.79 and 44.07 % for λ-MnO_2//λ-MnO_2, λ-MnO_2//AC and λ-MnO_2//$Ti_3C_2T_x$ SCs, respectively. The relatively higher rate performance of λ-MnO_2//$Ti_3C_2T_x$ MXene ASC is attributed to the good conducting behavior of the $Ti_3C_2T_x$ MXene negative electrode. The λ-MnO_2//$Ti_3C_2T_x$ MXene ASC showed a maximum energy density of 15.5 Wh kg^{-1} at the power density of 1100 W kg^{-1} with a wide potential window from 0 to 2.2 V. This value is higher than the values obtained for symmetric λ-MnO_2//λ-MnO_2 (7.3

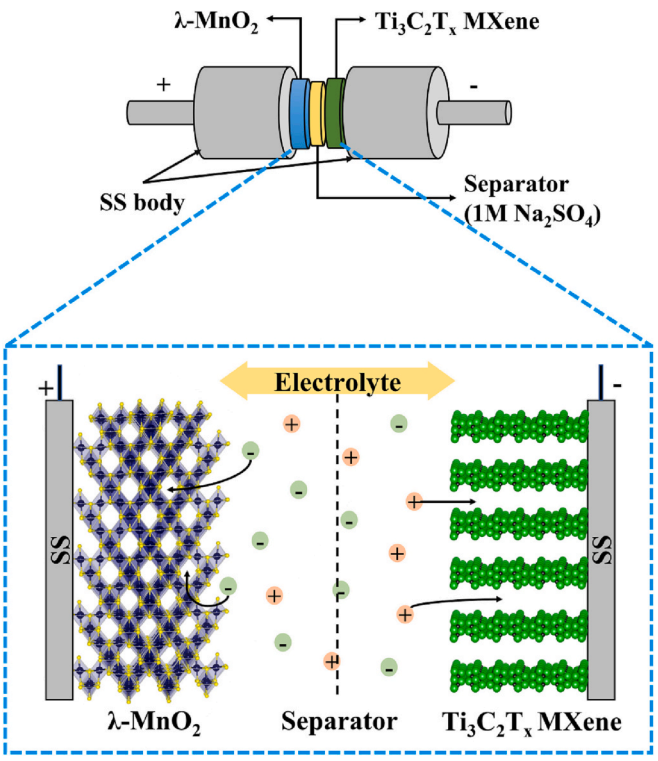

Fig. 7. Schematic diagram of λ-MnO_2//$Ti_3C_2T_x$ MXene ASC assembled using Swagelok cell.

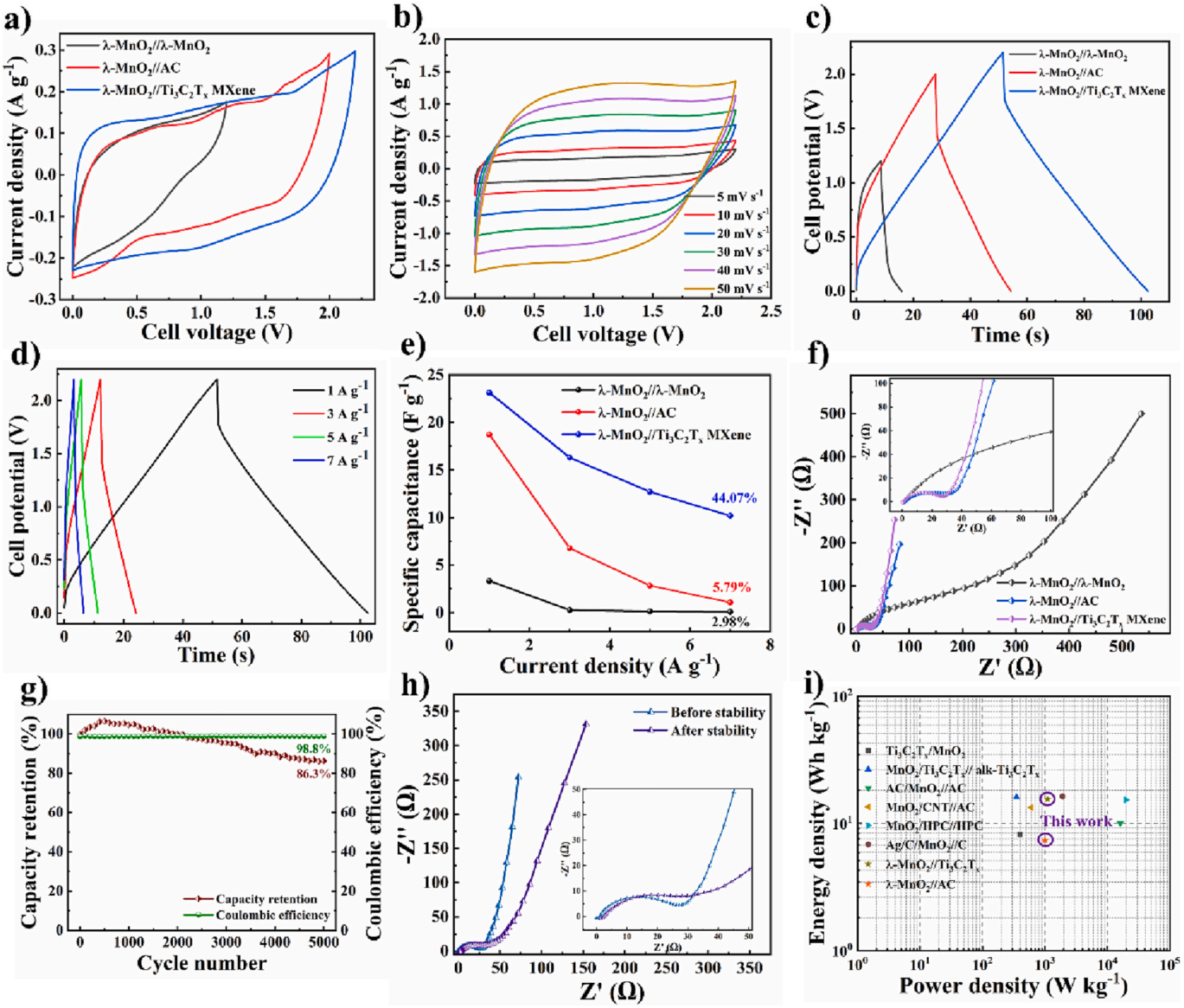

Fig. 8. (a) CV curves of λ-MnO_2//λ-MnO_2, λ-MnO_2//AC, and λ-MnO_2//$Ti_3C_2T_x$ MXene SCs at the scan rate of 5 mV s^{-1}; (b) CV curves of the λ-MnO_2//$Ti_3C_2T_x$ SC at different scan rates; c) GCD curves of λ-MnO_2//λ-MnO_2, λ-MnO_2//AC, and λ-MnO_2//$Ti_3C_2T_x$ MXene SCs at the current density of 1 A g^{-1}; (d) GCD curves of λ-MnO_2//$Ti_3C_2T_x$ MXene SC at different current densities; (e) The variation of specific capacitance versus current density of λ-MnO_2//λ-MnO_2, λ-MnO_2//AC, and λ-MnO_2//$Ti_3C_2T_x$ MXene SCs; (f) Nyquist plot for λ-MnO_2//λ-MnO_2, λ-MnO_2//AC, and λ-MnO_2//$Ti_3C_2T_x$ MXene SCs in the frequency range 0.01 Hz to 1 MHz (inset: zoomed high-frequency region); (g) The stability study of λ-MnO_2//$Ti_3C_2T_x$ MXene SC; (h) The Nyquist plots of λ-MnO_2//$Ti_3C_2T_x$ MXene SC before and after cycling; (i) Comparison of energy and power densities of both λ-MnO_2//AC and λ-MnO_2//$Ti_3C_2T_x$ MXene SCs with the values reported in literature.

Wh kg^{-1}@1000 W kg^{-1}) and asymmetric λ-MnO_2//AC (1.3 Wh kg^{-1}@1200.0 W kg^{-1}) SCs. The superior performance of MXene-based ASC may be mainly due to the high conducting nature of $Ti_3C_2T_x$ MXene, good specific capacitance and extended potential window of the device. To further shed light on the electrical properties of λ-MnO_2// λ-MnO_2, λ-MnO_2//AC, and λ-MnO_2//$Ti_3C_2T_x$ SCs, these devices were subjected to EIS analysis as shown in Fig. 8f. The estimated R_s and R_{ct} values are shown in Table S2. Since all SCs were fabricated with identical dimensions and the same electrolytic solution, the R_s values were similar, displaying the good conductivity of electrolyte/planar electrodes and small thicknesses of active material and separator. As compared to other SCs, the λ-MnO_2//$Ti_3C_2T_x$ ASC showed a very small value of R_s (0.61 Ω) which may be due to the relatively higher conductivity of $Ti_3C_2T_x$ MXene negative electrode. Besides, the highest R_{ct} value (184 Ω) of symmetric λ-MnO_2//λ-MnO_2 SC was owing to the poor conductivity of λ-MnO_2. The R_{ct} value of λ-MnO_2//$Ti_3C_2T_x$ ASC was smaller than the λ-MnO_2//AC ASC which can be ascribed to the excellent intrinsic conductivity of the $Ti_3C_2T_x$ MXene electrode. Also, the straight line in the low-frequency region for λ-MnO_2//$Ti_3C_2T_x$ ASC was steeper than that for symmetric λ-MnO_2//λ-MnO_2 and asymmetric λ-MnO_2//AC SCs, implying the capacitive character of the $Ti_3C_2T_x$ MXene based ASC. Furthermore, the stability of the λ-MnO_2//$Ti_3C_2T_x$ device was examined using the GCD technique for 5000 GCD cycles at the current density of 5 A g^{-1} (Fig. 8g), highlighting the capacitance retention of 86.3 % with the CE of ~99 % after 5000 cycles. The performance of MXene-based SC was found to be appreciable when compared with the other devices (Fig. S4). Furthermore, to understand the effect of cycling on the electrical properties of λ-MnO_2//$Ti_3C_2T_x$ MXene ASC, the EIS was performed before and after cycling as shown in Fig. 8h. The R_s value before and after cycling was reported as 0.6 and 1.7 Ω, depicting there is no significant change in the electrode and electrolyte resistance of the device. However, the R_{ct} value was

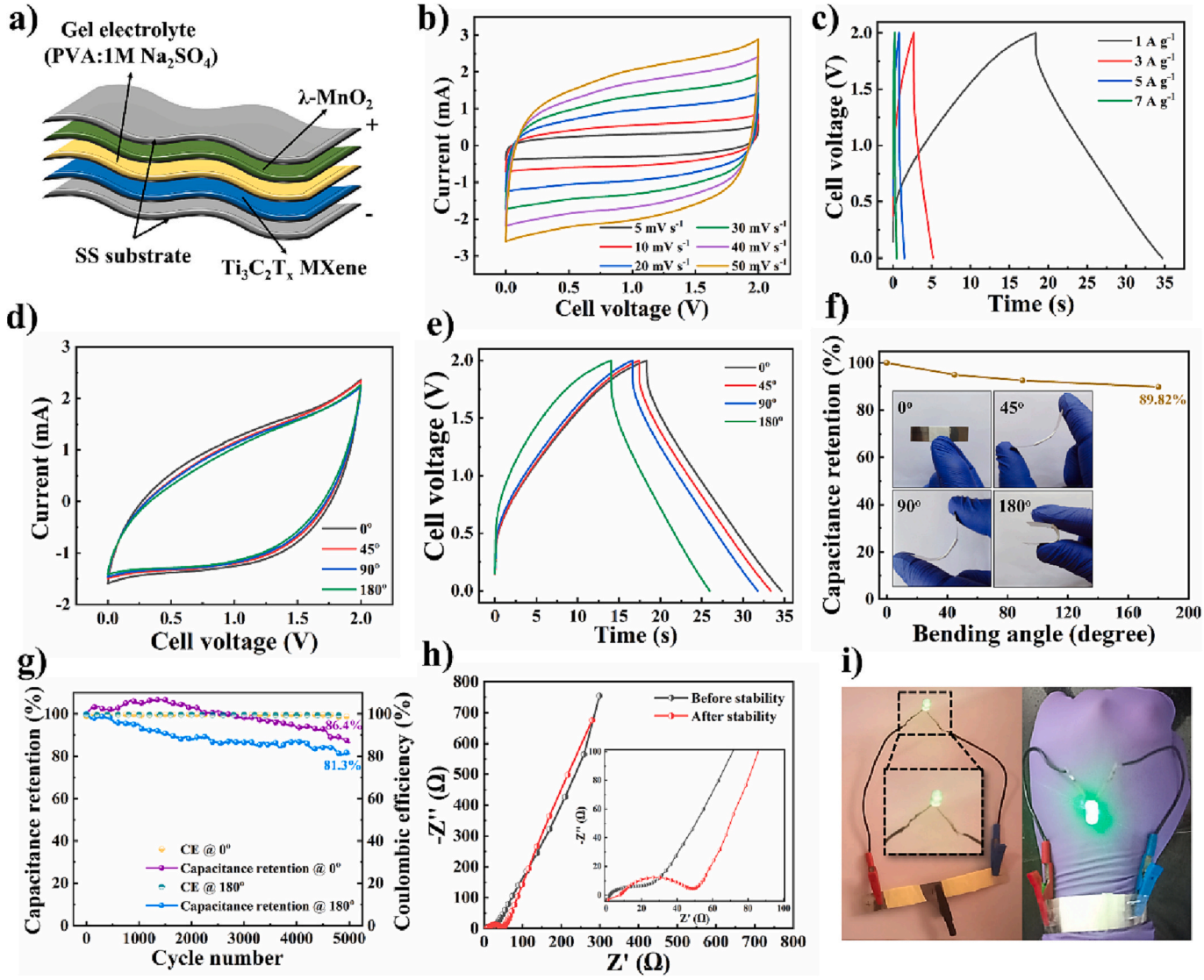

Fig. 9. (a) Schematic diagram of λ-MnO_2//$Ti_3C_2T_x$ MXene flexible SC; (b) CV curves of flexible λ-MnO_2//$Ti_3C_2T_x$ MXene SC at different scan rates; (c) GCD curves of flexible λ-MnO_2//$Ti_3C_2T_x$ MXene SC at different current densities; (d) CV curves of flexible λ-MnO_2//$Ti_3C_2T_x$ MXene SC at different bending angles; (e) GCD curves of flexible λ-MnO_2//$Ti_3C_2T_x$ MXene SC at different bending angles; (f) The variation of capacitance retention versus bending angle for flexible λ-MnO_2//$Ti_3C_2T_x$ MXene SC (inset: the photographs of flexible λ-MnO_2//$Ti_3C_2T_x$ MXene SC at various bending angles); (g) The stability study of flexible λ-MnO_2//$Ti_3C_2T_x$ MXene SC at 0 and 180° bending angles; (h) Nyquist plots for flexible λ-MnO_2//$Ti_3C_2T_x$ MXene SC before and after cycling (zoomed high-frequency region); (i) Demonstration of a glowing LED powered by flexible λ-MnO_2//$Ti_3C_2T_x$ MXene SCs.

increased from 26 to 35 Ω, indicating that the capacitance fading could be due to the increased charge transfer resistance. This increased charge transfer resistance may be attributed to the morphological changes of electrodes. To check these changes after cycling, the λ-MnO_2//$Ti_3C_2T_x$ MXene ASC was disassembled and cycled electrodes were subjected to FESEM analysis. As shown in Fig. S5, the morphology of λ-MnO_2 was significantly altered after cycling. However, the microstructure of $Ti_3C_2T_x$ MXene was well retained. The ED and PD values of λ-MnO_2//$Ti_3C_2T_x$ MXene and λ-MnO_2//AC ASCs were compared with the help of Ragone plot (Fig. 8i) and Table S3, showing excellent performance when compared with the reported SCs fabricated with MnO_2 and its composites shown.

To assess the applicability of the λ-MnO_2 and $Ti_3C_2T_x$ electrodes in the flexible SCs, the flexible ASC of thickness 0.247 mm was fabricated using λ-MnO_2 as the positive electrode, $Ti_3C_2T_x$ MXene as the negative electrode and PVA: Na_2SO_4 polymer gel as an electrolyte (Fig. 9a). The CV curves of fabricated flexible λ-MnO_2//$Ti_3C_2T_x$ MXene ASC at different scan rates with the operating potential of 2 V are shown in Fig. 9b, demonstrating quasi-rectangular shape which may be due to the pseudocapacitive nature of λ-MnO_2 and $Ti_3C_2T_x$ electrodes. Moreover, the flexible λ-MnO_2//$Ti_3C_2T_x$ MXene ASC device was examined using the GCD technique at different current densities as shown in Fig. 9c, revealing maximum volumetric ED of 606 μWh cm^{-3} at a PD of 130.4 mW cm^{-3}. Also, it shows an areal ED of 39.9 μWh cm^{-2} at a PD of 8586 μW cm^{-2}. The flexibility performance of the flexible λ-MnO_2//$Ti_3C_2T_x$ MXene ASC was explored by recording CV and GCD curves at different bending angles (Fig. 9d-f), depicting excellent capacitance retention of 89.8 % even at the bending angle of 180°. To test rate capabilities at different bending angles, GCD curves at current densities ranging from 1 to 7 A g^{-1} were recorded (Fig. S6), demonstrating a decrement in the rate capability at extreme bending condition of 180°. However, the rate capabilities are appreciable at moderate bending conditions. The cyclic stability of the flexible device at 0 and 180° bending angles was examined for 5000 GCD cycles at 5 A g^{-1}, exhibiting appreciable capacitance retention of 86.4 and 81.3 % respectively, along with CE of ~99 % (Fig. 9g). Fig. 9h shows the Nyquist plots for flexible λ-MnO_2//$Ti_3C_2T_x$

ASC before and after 5000 GCD cycles. The estimated R_s and R_{ct} values before and after cycling were found to be 2, 4 Ω and 18, 43 Ω, respectively. The increase in R_s, as well as R_{ct} values, may be attributed to the increased ionic resistance of polymer gel electrolyte that might be resulted due to the evaporation of water from the gel electrolyte. To demonstrate the wearability, the flexible λ-MnO_2//$Ti_3C_2T_x$ MXene ASC was fixed on the human wrist which was found to be glowing LED for 5 min after charging for 1 min (Fig. 9i). Thus, this study concludes that the λ-MnO_2 prepared through a simple and scalable co-precipitation method exhibits a promising role in $Ti_3C_2T_x$ MXene-based asymmetric flexible supercapacitor.

4. Conclusion

In summary, the nanoplates-like λ-MnO_2 was successfully synthesized using a facile, single-step and scalable co-precipitation method. This λ-MnO_2 nanoplates-like material depicted a high specific surface area of 64.13 m^2 g^{-1} with a meso-macro porous structure. It displayed a maximum specific capacitance of 288.5 F g^{-1} at the scan rate of 5 mV s^{-1}. Moreover, the λ-MnO_2//$Ti_3C_2T_x$ ASC device exhibited a high ED of 15.5 Wh kg^{-1} at the PD of 1100 W kg^{-1}. Besides, it exhibited excellent cyclic stability up to 86.3 % with a CE of 98.8 % after 5000 cycles. The flexible λ-MnO_2//$Ti_3C_2T_x$ MXene ASC demonstrated an appreciable potential window of 2 V with a superior areal ED of 39.9 μWh cm^{-2} at PD of 8586.4 μW cm^{-2}. Therefore, the ASC fabricated from a synergic effect between all pseudocapacitive λ-MnO_2 nanoplates and 2D-$Ti_3C_2T_x$ MXene electrodes can be considered a favorable candidate for flexible electrochemical energy storage.

CRediT authorship contribution statement

Thanigai Vetrikarasan: Conceptualization, Methodology, Writing - review & editing.

Abhijith R Nair: Investigation, Results interpretation.

T. Karthick: Computational analysis, Results interpretation.

Surendra K Shinde: Review, Results interpretation, Validation, characterization.

Dae-Young Kim: Conceptualization, Validation, Characterization.

Shilpa N Sawant: Validation, Conceptualization, Supervision,

Ajay D Jagadale: Review & Editing, Supervision, Lab facilitation, Funding acquisition.

Declaration of competing interest

The authors declare that they have no known competing financial interests or personal relationships that could have appeared to influence the work reported in this paper.

Data availability

Data will be made available on request.

Acknowledgment

ADJ is grateful to the Department of Science and Technology (DST), Govt. of India for financial assistance under the DST INSPIRE Faculty scheme [DST/INSPIRE/04/2017/002737], DAE-BRNS Mumbai for financial support through Project No. 58/14/06/2022-BRNS/37040 for the 2022–2025 and Fund for Improvement of S&T Infrastructure (FIST) [SR/FST/PS-1/2020/135] scheme.

Appendix A. Supplementary data

Supplementary data to this article can be found online at https://doi.org/10.1016/j.est.2023.108403.

References

[1] Poonam, K. Sharma, A. Arora, S.K. Tripathi, Review of supercapacitors: materials and devices, J. Energy Storage 21 (2019) 801–825, https://doi.org/10.1016/j.est.2019.01.010.

[2] L. Zhang, X. Hu, Z. Wang, F. Sun, D.G. Dorrell, A review of supercapacitor modeling, estimation, and applications: a control/management perspective, Renew. Sust. Energ. Rev. 81 (2018) 1868–1878, https://doi.org/10.1016/j.rser.2017.05.283.

[3] K.V.G. Raghavendra, R. Vinoth, K. Zeb, C.V.V. Muralee Gopi, S. Sambasivam, M. R. Kummara, I.M. Obaidat, H.J. Kim, An intuitive review of supercapacitors with recent progress and novel device applications, J. Energy Storage 31 (2020), 101652, https://doi.org/10.1016/j.est.2020.101652.

[4] A. Muzaffar, M.B. Ahamed, K. Deshmukh, J. Thirumalai, A review on recent advances in hybrid supercapacitors: design, fabrication and applications, Renew. Sust. Energ. Rev. 101 (2019) 123–145, https://doi.org/10.1016/j.rser.2018.10.026.

[5] W. Raza, F. Ali, N. Raza, Y. Luo, K.-H. Kim, J. Yang, S. Kumar, A. Mehmood, E. E. Kwon, Recent advancements in supercapacitor technology, Nano Energy 52 (2018) 441–473, https://doi.org/10.1016/j.nanoen.2018.08.013.

[6] M.M. Baig, I.H. Gul, S.M. Baig, F. Shahzad, 2D MXenes: synthesis, properties, and electrochemical energy storage for supercapacitors – a review, J. Electroanal. Chem. 904 (2022), 115920, https://doi.org/10.1016/j.jelechem.2021.115920.

[7] S. Venkateshalu, G. Subashini, P. Bhardwaj, G. Jacob, R. Sellappan, V. Raghavan, S. Jain, S. Pandiaraj, V. Natarajan, B.A.M. Al Alwan, M.K.M. Al Mesfer, A. Alodhayb, M. Khalid, A.N. Grace, Phosphorene, antimonene, silicene and siloxene based novel 2D electrode materials for supercapacitors-a brief review, J. Energy Storage 48 (2022), 104027, https://doi.org/10.1016/j.est.2022.104027.

[8] N. Choudhary, C. Li, J. Moore, N. Nagaiah, L. Zhai, Y. Jung, J. Thomas, Asymmetric supercapacitor electrodes and devices, Adv. Mater. 29 (2017) 1605336, https://doi.org/10.1002/adma.201605336.

[9] S. Korkmaz, F.M. Tezel, İ.A. Kariper, Synthesis and characterization of GO/V2O5 thin film supercapacitor, Synth. Met. 242 (2018) 37–48, https://doi.org/10.1016/j.synthmet.2018.05.002.

[10] K. Panigrahi, P. Howli, K.K. Chattopadhyay, 3D network of V2O5 for flexible symmetric supercapacitor, Electrochim. Acta 337 (2020), 135701, https://doi.org/10.1016/j.electacta.2020.135701.

[11] S. Yao, F. Qu, G. Wang, X. Wu, Facile hydrothermal synthesis of WO3 nanorods for photocatalysts and supercapacitors, J. Alloys Compd. 724 (2017) 695–702, https://doi.org/10.1016/j.jallcom.2017.07.123.

[12] M. Hu, H. Zhang, T. Hu, B. Fan, X. Wang, Z. Li, Emerging 2D MXenes for supercapacitors: status, challenges and prospects, Chem. Soc. Rev. 49 (2020) 6666–6693, https://doi.org/10.1039/D0CS00175A.

[13] R. Garg, A. Agarwal, M. Agarwal, A review on MXene for energy storage application: effect of interlayer distance, Mater. Res. Express. 7 (2020), 022001, https://doi.org/10.1088/2053-1591/ab750d.

[14] R.C. Rohit, A.D. Jagadale, S.K. Shinde, D.-Y. Kim, MXene (Ti3C2Tx) modified α-Co(OH)2 battery-type cathode and highly capacitive binder-free Ti3C2Tx anode for high-performance electrochemical hybrid capacitor, 2D, Mater. 9 (2022), 045031, https://doi.org/10.1088/2053-1583/ac9191.

[15] Y. Wei, M. Zheng, W. Luo, B. Dai, J. Ren, M. Ma, T. Li, Y. Ma, All pseudocapacitive MXene-MnO2 flexible asymmetric supercapacitor, J. Energy Storage 45 (2022), 103715, https://doi.org/10.1016/j.est.2021.103715.

[16] N.S. Shaikh, S.B. Ubale, V.J. Mane, Jasmin S. Shaikh, Vaibhav C. Lokhande, S. Praserthdam, C.D. Lokhande, P. Kanjanaboos, Novel electrodes for supercapacitor: conducting polymers, metal oxides, chalcogenides, carbides, nitrides, MXenes, and their composites with graphene, J. Alloys Compd. 893 (2022), 161998, https://doi.org/10.1016/j.jallcom.2021.161998.

[17] T.S. Bhat, S.A. Jadhav, S.A. Beknalkar, S.S. Patil, P.S. Patil, MnO2 core-shell type materials for high-performance supercapacitors: a short review, Inorg. Chem. Commun. 141 (2022), 109493, https://doi.org/10.1016/j.inoche.2022.109493.

[18] Y. Zhang, C. Yuan, K. Ye, X. Jiang, J. Yin, G. Wang, D. Cao, An aqueous capacitor battery hybrid device based on Na-ion insertion-deinsertion in λ-MnO2 positive electrode, Electrochim. Acta 148 (2014) 237–243, https://doi.org/10.1016/j.electacta.2014.10.052.

[19] Modified MAX Phase synthesis for environmentally stable and highly conductive Ti3C2 MXene|ACS nano, (n.d.). https://pubs.acs.org/doi/10.1021/acsnano.0c08357 (accessed May 2, 2023).

[20] Understanding the impact of the morphology, phase structure, and mass fraction of MnO2 within MnO2/reduced graphene oxide composites for supercapacitor applications J. Phys. Chem. C, (n.d.). https://pubs.acs.org/doi/full/10.1021/acs.jpcc.2c02731 (accessed February 6, 2023).

[21] J. Wang, X. Guo, R. Cui, H. Huang, B. Liu, Y. Li, D. Wang, D. Zhao, J. Dong, S. Li, B. Sun, MnO2/porous carbon nanotube/MnO2 nanocomposites for high-performance supercapacitor, ACS Appl. Nano Mater. 3 (2020) 11152–11159, https://doi.org/10.1021/acsanm.0c02163.

[22] C. Li, Z. Yu, H. Liu, L. Kong, Dandelion-like α-MnO2 hollow spheres with superior catalytic performance for Li-O2 batteries by a facile in situ pyrolysis, J. Mater. Sci. 53 (2018) 14525–14535, https://doi.org/10.1007/s10853-018-2629-1.

[23] F. Liao, X. Han, D. Cheng, Y. Zhang, X. Han, C. Xu, H. Chen, MnO2 hierarchical microspheres assembled from porous nanoplates for high-performance supercapacitors, Ceram. Int. 45 (2019) 1058–1066, https://doi.org/10.1016/j.ceramint.2018.09.285.

[24] P. Giannozzi, S. Baroni, N. Bonini, M. Calandra, R. Car, C. Cavazzoni, D. Ceresoli, G.L. Chiarotti, M. Cococcioni, I. Dabo, A.D. Corso, S. de Gironcoli, S. Fabris, G. Fratesi, R. Gebauer, U. Gerstmann, C. Gougoussis, A. Kokalj, M. Lazzeri,

L. Martin-Samos, N. Marzari, F. Mauri, R. Mazzarello, S. Paolini, A. Pasquarello, L. Paulatto, C. Sbraccia, S. Scandolo, G. Sclauzero, A.P. Seitsonen, A. Smogunov, P. Umari, R.M. Wentzcovitch, QUANTUM ESPRESSO: a modular and open-source software project for quantum simulations of materials, J. Phys. Condens. Matter 21 (2009), 395502, https://doi.org/10.1088/0953-8984/21/39/395502.

[25] Nanomaterials|Free Full-Text|A Hollow-Structured Manganese Oxide Cathode for Stable Zn-MnO2 Batteries, (n.d.). https://www.mdpi.com/2079-4991/8/5/301 (accessed February 6, 2023).

[26] Physisorption of gases, with special reference to the evaluation of surface area and pore size distribution (IUPAC Technical Report), (n.d.). https://www.degruyter.com/document/doi/10.1515/pac-2014-1117/html?lang=en (accessed February 6, 2023).

[27] H.B. Li, M.H. Yu, F.X. Wang, P. Liu, Y. Liang, J. Xiao, C.X. Wang, Y.X. Tong, G. W. Yang, Amorphous nickel hydroxide nanospheres with ultrahigh capacitance and energy density as electrochemical pseudocapacitor materials, Nat. Commun. 4 (2013) 1894, https://doi.org/10.1038/ncomms2932.

[28] B. Chettiannan, A.K. Srinivasan, G. Arumugam, S. Shajahan, M.A. Haija, R. Rajendran, Incorporation of α-MnO2 nanoflowers into zinc-terephthalate metal–organic frameworks for high-performance asymmetric supercapacitors, ACS Omega 8 (2023) 6982–6993, https://doi.org/10.1021/acsomega.2c07808.

[29] X. Zhang, X. Sun, H. Zhang, C. Li, Y. Ma, Comparative performance of birnessite-type MnO2 nanoplates and octahedral molecular sieve (OMS-5) nanobelts of manganese dioxide as electrode materials for supercapacitor application, Electrochim. Acta 132 (2014) 315–322, https://doi.org/10.1016/j.electacta.2014.03.176.

[30] Physical interpretations of electrochemical impedance spectroscopy of redox active electrodes for electrical energy storage J. Phys. Chem. C, (n.d.). https://pubs.acs.org/doi/full/10.1021/acs.jpcc.8b05241 (accessed February 6, 2023).

[31] C. Lei, F. Markoulidis, Z. Ashitaka, C. Lekakou, Reduction of porous carbon/Al contact resistance for an electric double-layer capacitor (EDLC), Electrochim. Acta 92 (2013) 183–187, https://doi.org/10.1016/j.electacta.2012.12.092.

[32] L. Lin, S. Chen, X. Qi, J. Yao, L. Meng, W. Chen, h-BN doped β-MnO2 nanobelts composite as superior electrode materials for supercapacitors, Mater. Lett. 328 (2022), 133209, https://doi.org/10.1016/j.matlet.2022.133209.

[33] C. Yang, W. Que, X. Yin, Y. Tian, Y. Yang, M. Que, Improved capacitance of nitrogen-doped delaminated two-dimensional titanium carbide by urea-assisted synthesis, Electrochim. Acta 225 (2017) 416–424, https://doi.org/10.1016/j.electacta.2016.12.173.

[34] S.B. Aziz, E.M.A. Dannoun, A.R. Murad, K.H. Mahmoud, M.A. Brza, M.M. Nofal, K. A. Elsayed, S.N. Abdullah, J.M. Hadi, M.F.Z. Kadir, Influence of scan rate on CV pattern: electrical and electrochemical properties of plasticized methylcellulose: dextran (MC:Dex) proton conducting polymer electrolytes, Alex. Eng. J. 61 (2022) 5919–5937, https://doi.org/10.1016/j.aej.2021.11.020.

[35] M. Wang, X. Liu, B. Qin, Z. Li, Y. Zhang, W. Yang, H. Fan, In-situ etching and ion exchange induced 2D-2D MXene@Co9S8/CoMo2S4 heterostructure for superior Na+ storage, Chem. Eng. J. 451 (2023), 138508, https://doi.org/10.1016/j.cej.2022.138508.

[36] C. Li, J. Wang, Y. Yan, P. Huo, X. Wang, MOF-derived NiZnCo-P nano-array for asymmetric supercapacitor, Chem. Eng. J. 446 (2022), 137108, https://doi.org/10.1016/j.cej.2022.137108.